A DFT-D2 Study of the Adsorption and Dissociation of Water on Clean and Oxygen-covered {001} and {011} Surfaces of Mackinawite (FeS)

N. Y. Dzade[1], A. Roldan[2] and N.H de Leeuw[1, 2]*

[1]Department of Earth Sciences, Utrecht University, Princetonplein 9, 3584 CC, Utrecht, The Netherlands `

[2]School of Chemistry, Cardiff University, Main Building, Park Place, CF10 3AT, Cardiff, United Kingdom

E-mail: N.Y.Dzade@uu.nl (N.Y.D); N.H.Deleeuw@uu.nl (N.H.dL)

ABSTRACT

We present a dispersion-corrected density functional theory study of the adsorption and dissociation reactions of oxygen and water on the {001} and {011} surfaces of mackinawite (FeS). A chemical picture of the initial steps of the mackinawite {001} and {011} surfaces oxidation process in the presence of oxygen and water is presented in the present investigation. Our results show that, while water interacts weakly with the Fe ions on both surfaces and only oxidizes them to some extent, atomic and molecular oxygen interact strongly with the FeS{011} surface cations by drawing significant charge from them, thereby oxidizing them from Fe^{2+} to Fe^{3+} formal oxidation state. We show from our calculated adsorption energies and activation energy barriers for the dissociation of H_2O on the clean and oxygen-covered FeS surfaces, that pre-adsorbed oxygen could easily activate the O–H bond and facilitate the dissociation of H_2O to ferric-hydroxy, Fe^{3+}–OH^- on FeS{011}, and to zero-valent sulfur-hydroxyl, S^0–OH^- on FeS{001}. With the aid of pre-adsorbed O atom, the activation energy barrier for dissociating hydrogen atom from H_2O decreases from 1.73 eV to 1.19 eV on the FeS{001}, and from 0.83 eV to 0.14 eV on the FeS{011}. These findings provide molecular-level insight into the mechanisms of mackinawite oxidation, and are consistent with experimental results, which have shown that oxygen and water are necessary for the oxidation process of mackinawite and its possible transformation to pyrite *via* greigite.

TABLE OF CONTENT (TOC) IMAGE

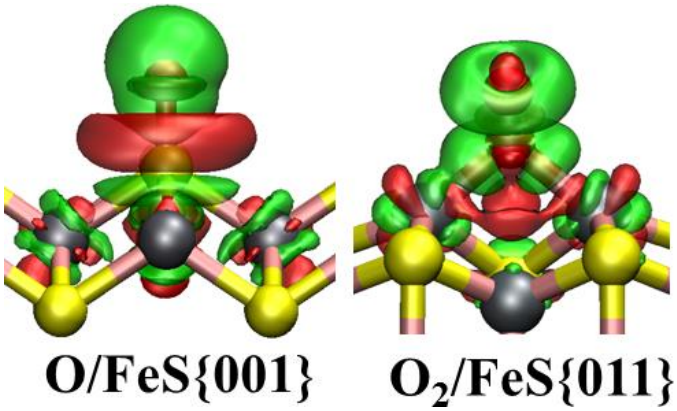

1. INTRODUCTION

Iron sulfides have attracted significant scientific interest in recent times owing to their low cost, natural abundance, and unique physical and chemical properties which make them strong candidate materials in technological applications such as solar cells,[1–7] solid-state batteries,[8–10] and heterogenoues catalysis.[11–15] Iron sulfides have also been suggested to play an important catalytic role in a surface-mediated chemoautrophic Origin-of-Life hypothesis.[17–22] Due to thier surface reactivity, iron sulfides have also been extensively employed in environmental applications for the sequestration of trace elements (eg. As, Se and Cr) through adsorption[23, 24] or oxidative dissolution[25–27] processes. Owing to the multiple oxidation states of iron, a wide range of naturally occurring iron sulfides exists, including mackinawite (FeS_{1-x}), troilite (FeS), pyrrhotite ($Fe_{1-x}S$), greigite (Fe_3S_4), and pyrite (FeS_2).[28]

When in contact with oxygen and water, iron sulfides are easily oxidized,[29-34] making them difficult to characterize, which has remained the primary problem that limits the potential applications of these materials severely.[35] Protection of iron sulfide surfaces against unwanted oxidation requires a comprehensive understanding of the fundamental reaction mechanisms of environmentally ubiquitous species such as oxygen and water. Earlier

experimental investigations of the interaction of water and oxygen with iron sulfides have focused on hydration[32, 36–38] and oxidation[39–42] of pyrite surfaces. Furthermore, significant information is found in the literature regarding the oxidation and chemistry of different stoichiometric and defective pyrite surfaces using *ab initio* theoretical calculations.[43–49]

Despite extensive studies on the interaction of oxygen with pyrite, there exist limited investigations that characterize the interactions of oxygen and water with other iron sulfides surfaces[16,50, 51] and the detail mechanism of the early oxidation of mackinawite has not yet been established. Mackinawite easily transforms to pyrite via greigite, but the transformation was shown to be possible only in the presence of oxygen or some other oxidants.[29] Berner *et al.*[30] in his study of the formation of iron sulfides from aqueous solutions at low temperature and atmospheric pressure also reported that oxygen was necessary to the oxidation process. Boursiquot *et al.*[52] studied the gradual oxidation processes of dry mackinawite using a range of experimental techniques including X-ray diffraction (XRD), transmission electron microscopy (TEM) and transmission Mössbauer spectroscopy (TMS). The Mössbauer spectra of their samples oxidised in air appeared rather too complex for interpretation. Nevertheless, they found that the mackinawite samples reacted mainly with adsorbed O_2 to form elemental sulfur and magnetite.[52] A theoretical understanding of the fundamental adsorption and reaction processes of O_2 and H_2O on mackinawite surfaces is, however, still lacking.

In this study, we contribute molecular-level insight into the mechanisms of the early oxidation of mackinawite by comprehensive dispersion-corrected density-functional theory (DFT-D2) calculations of the reactions of O_2 and H_2O with the {001} and {011} surfaces, considering both molecular and dissociative adsorption. The electronic and vibrational properties of the adsorbed O_2 and H_2O molecules are discussed and their possible dissociation pathways have been determined.

2. COMPUTATIONAL DETAILS

All geometry optimizations were performed using the Vienna *Ab-initio* Simulation Package (VASP) with plane-wave basis set.[53–55] Long range dispersion forces were accounted for within the Grimme scheme (DFT-D2),[56] which is crucial for a proper description of the interlayer interactions in two-dimensional layered materials and the adsorption systems.[12] The electronic exchange–correlation potential was calculated using the Generalized Gradient Approximation (GGA) with PW91 functional.[57] The plane-wave energy cut-off was 400 eV for all calculations and within each self-consistency cycle, the total energy was converged to within 10^{-6} eV and the forces in ionic relaxations were converged to within 0.01 eV/Å. Test calculations with a higher energy cut-offs led to an energy difference smaller than 0.03 eV adsorbate-substrate system. For bulk and surface calcualtions, the Brillouin zone was sampled using a 11×11×11 and 5×5×1, respectively, Monkhorst-Pack[59] *k*-point mesh.

The mackinawite {001} and {011} surfaces were created with METADISE code[60] from the fully optimized bulk structure. Surface terminations with atomic layer stacking resulting in a zero dipole moment perpendicular to the surface plane were considered for the adsorption calculations.[61] Different slab and vacuum thicknesses were tested for the different surfaces until convergence within 1 meV per cell was achieved. The adsorption calculations were carried out on FeS{001}-*p*(2×2) and FeS{001}-*p*(3×1) supercells such that the effective coverage was 0.25 ML, and in each supercell a vacuum region of size 15 Å was added in the *c*-direction to avoid interaction between consecutive slabs. To determine the optimum adsorption sites and geometries, the atoms of the adsorbate and the topmost three layers of the slab were allowed to relax unconstrainedly until residual forces on all atoms had reached 0.01 eV/Å. The adsorption energy (E_{ads}) was defined as follows:

$$E_{ads} = E_{adsorbate-surface} - (E_{surface} + E_{adsorbate}) \quad (1)$$

where $E_{adsorbate + surface}$ is the total energy of the adsorbate–substrate system in the equilibrium state, $E_{surface}$ the total energy of the substrate alone, and $E_{adsorbate}$ the total energy of the free adsorbate alone. A negative value of E_{ads} then indicates an exothermic and favourable adsorption process, whereas a positive value indicates an endothermic and unfavourable adsorption process. The reference energy for atomic oxygen (O) is taken as half the energy of isolated oxygen molecule (O_2) calculated in a cubic cell of size 15 Å, sampling only the Γ-point of the Brillouin zone. Bader charge analysis using the code developed by Henkelman and co-workers[62] was used to quantify the charge transfer between the FeS surfaces and the adsorbing species.The climbing-image nudged elastic band (cNEB) method[63, 64] was used to identify the transition states and reaction barriers for the dissociation reactions of O_2 and H_2O on the FeS surfaces. The saddle points thus located were confirmed by vibrational frequency calculations, in which only one imaginary frequency is obtained corresponding to the reaction coordinate.

3. RESULTS AND DISCUSSIONS

3.1 Bulk and surface characterisation

As schematically shown in **Figure 1a**, mackinawite (FeS) adopts the tetragonal structure, space group P4/nmm. The crystal structure is simple, with the iron atoms coordinated tetrahedrally by sulphur on a square lattice, to form edge-sharing tetrahedral layered sheets stacked along the *c*-axis and stabilized by van der Waals forces (vdW).[65-67] The iron atom are arranged in a square-planar coordination at an Fe–Fe distance of 2.597 Å.[65] By performing full relaxation calculations, our calculated lattice parameters for the strain-free FeS structure are $a = b = 3.587$ Å, $c = 4.908$ Å, with c/a ratio = 1.368 Å, which compares well with the range of experimental[31,65, 66, 69, 70] values reported in **Table 1**. The inclusion of van der Waals dispersive interactions is found to improve the prediction of

interlayer separation distance of FeS to within 1−3 % of experiment, compared to the 11 % overestimation from standard DFT calculations.[58, 71] Our calculated electronic density of states (**Figure 1b**), shows metallic character for FeS, with the electronic states of the Fe *d*-orbitals dominating the regions around the Fermi level, in agreement with the metallic nature deduced from experiments,[72] and earlier DFT calculations.[58, 73, 74]

From the fully optimized tetragonal FeS structure, we have cut and modelled the low index {001} and {011} families of surfaces, which are the dominant growth surfaces expressed in the morphology of the mackinawite nanocrystals.[12, 58, 75] The relaxed structures of the {001} and {011} surfaces and the corresponding different adsorption sites explored in this study are schematically shown in **Figure 2**. The relaxed surface energies of the {001} and {011} surfaces are calculated at 0.19 J m^{-2} and 0.95 J m^{-2}, respectively. The {001} surface is by far the most stable surface of FeS because its creation only involves breaking the weak vdW interactions between the sulfide layers which results in negligible relaxation of the surface species. This result is consistent with the experimental results of Ohfuji and Rickard *et al.*[75] on FeS nanocrystals and the theoretical interatomic potential study[58] of FeS surface structures.

3.2 Oxygen and water geometry parameters

Prior to the adsorption of O_2 and H_2O, we have calculated the reference energies, bond length (*d*), and stretching vibrational frequencies (υ) of H_2O and O_2 in its spin triplet and compared them with earlier theoretical results and available experimental data. The calculated results for O_2 are d(O−O) =1.24 Å and υ(O−O) =1545 cm^{-1}, which agree well with the experimental values of 1.21 Å,[76] and 1555 cm^{-1},[77] as well as with other DFT results.[78, 79] The d(O−H) and α(H-O-H) angle of water are calculated to be 0.972 Å and 104.7°

respectively, and the calculated asymmetric and symmetric stretching vibrational frequencies are 3713 and 3623 cm^{-1}, all of which in good agreement with experimental values.[80, 81]

3.3 Adsorption of atomic and molecular oxygen on FeS{001} surface

For adsorption of atomic oxygen on the FeS{001} surface, three distinct adsorption sites were examined as presented in **Figure 1b**. The calculated adsorption energies and the optimized interatomic bond distances are summarized in **Table 2**. When placed at top-Fe site, it was found that the initial configuration is converted to top-S configuration after optimization (**Figure 3 A1**). The calculated adsorption energies of O at top-S (**Figure 3 A1**) and 4-fold-bridge-Fe (**Figure 3 A2**) sites are −1.02 eV and −0.11 eV, respectively, which indicates that top-S site is the most stable and active site for atomic O adsorbed on the FeS{001} surface. The preference of the O atom adsorption at the S site compared to Fe can be attributed to the shielding of the inner Fe atoms by the terminating S ions, which prevents any direct interaction between O atom and Fe.

For the adsorption of molecular oxygen (O_2/FeS{001} system), we have considered two adsorption modes; the end-on type, where O_2 vertically binds to the surface atom, and a side-on type, where O_2 binds parallel to the surface atom. When adsorbed side-on at top-Fe site (**Figure 3M1**), a positive adsorption energy of +1.04 eV was calculated, which suggests a highly unfavourable adsorption mode. The surface Fe with the Fe−O bonds is pulled upwards by 0.58 Å in the direction perpendicular to the surface from its initial surface position, causing significant distortion of the surface structure around the Fe adsorption site (**Figure 3M1**), which explains the unstable adsorption. In the case of O_2 adsorbed end-on at top-S, it is found that the the O_2 molecule moved away from the initial top-S site during geometry optimization until the distances between the oxygen atom pointing towards the surface S and Fe ions are 3.434 Å and 3.783 Å, respectively (**Figure 3M2**), releasing an adsorption energy

of 0.12 eV. We have also considered a side-on O_2 adsorption at top-S site but found that is it converted to the end-on top-S configuration after geormetry optimization. Similar adsorption characteristics are calculated for O_2 adsorbed end-on (**Figure 3M3**) and side-on at the 4-fold-bridge-Fe (**Figure 3M4**) sites. The adsorption energies of the end-on and side-on configurations of O_2 adsorbed at the 4-fold-bridge-Fe site are −0.13 eV and −0.16 eV, respectively, with the shortest O−Fe; O−S interatomic distances calculated at 3.768; 3.157 Å and 3.698; 3.125 Å, respectively (**Table 2**). In agreement with the weak O_2 interactions predicted in **Figures 3**(**M2**, **M3**, and **M4**), no significant changes are observed in the O−O bond length relative to the gas phase molecule. Further insight into the nature of bonding of the atomic and molecular oxygen on the {001} surface was gained from the partial DOS projected on the interacting surface S *p*-states and O *p*-states for lwest-energy adsorption configurations as shown in **Figure 4**. Compared to the weakly physisorbed molecular oxygen (E_{ads} =−0.16 eV), in which the interacting surface S ions remained negatively charged, the strong interaction of atomic oxygen (E_{ads} =−1.02 eV) with the surface S ion causes disappearance or reduction of S states around the Fermi level, due to strong hybridization between S-*p* and O-*p* states. Consistent with the strong interaction in the O/FeS{001} system, our Bader population analyses reveal that the adsorbed O atom draws a charge of 1.85 e^- from the bound S ions, which results in its significant oxidation from a negatively charge state (−0.81 e^-) to a positively charged state (+0.95 e^-). Negligible charge transfer is observed for the O_2/FeS{001} complex, which is consistent with the physisorption and the topmost S ions remained negatively charged (−0.81 e^-). The corresponding electronic density resdistribution due to the interactions within the adsorbate-substrate systems is revealed by the isosurface of the differential electron density contour plots (**Figure 4 (b & d)**).

The dissociative adsorption of O_2 on the FeS{001} is found to be highly exothermic (E_{ads} = −1.88 eV), with a small activation barrier of only 0.45 eV, which suggests that the

FeS{001} favours dissociative O_2 adsorption rather than molecular adsorption. The dissociated O ions, which adsorb preferentially at top-S site (**Fgure 3D1**), draw a comibed charge of 3.64 e^- from the interacting surface S ions, resulting in their significant oxidation, with the S ions becoming positively charged (+0.95 e^-) compared to the negative charged of −0.81 e^- on the clean surface.

3.4 Adsorption of atomic and molecular oxygen on FeS{011} surface

Two distinct adsorption sites as presented in **Figure 2d** are examined for the adsorption of atomic O and molecular O_2 on the FeS{011} surface. Summarized in **Table 2** are the calculated adsorption energies, the optimized interatomic bond distances and Bader charges for adsorbed species. O adsorbed at the top-Fe-site (**Figure 5A2**) is found to bound 0.16 eV more strongly than at the bridge site (**Figure 5A1**), which is consistent with the shorter Fe−O bond calculated for the top-Fe (1.61 Å) than the bridge-Fe (1.84 Å) sites, as well as the larger charge drawn by the adsorbed O at top-Fe (0.67 e^-) than bridge-Fe (0.63 e^-) sites. No stable adsorption structure of atomic O was obtained at the S site on the FeS{011} surface as its initial configuration is converted to bridge-Fe site during energy minimization. The top and bridge Fe ions to which the atomic O is bound are pulled upwards in the direction perpendicular to the surface by 0.16 Å and 0.09 Å, respectively, while the unbound Fe sink into the surface by 0.14 Å.

For molecular O_2 adsorption on the FeS{011}, three adsorption configurations are obtained with the O_2 molecule binding: end-on at bridge-Fe-site (**Figure 5M1**), top-Fe-site (**Figure 5M2**), and side-on at top-Fe site (**Figure 5M3**). Listed in **Table 2** are the calculated adsorption energies and relevant interatomic bond distances. The adsorption energy for O_2 adsorbed end-on at bridge-Fe-site, top-Fe-site, and side-on at top-Fe-site are, respectively, calculated to be −0.98, −1.56, and −1.75 eV on the relaxed surface, which indicates that the

side-on O_2 configuration is energetically more favoured than the end-on configurations, although all adsorptions are highly exothermic. The interatomic Fe−O; O−O bond distances for O_2 bound end-on at the bridge and top-Fe sites are calculated to be 2.031 Å; 1.30 Å and 1.718 Å; 1.34 Å, respectively. For the side-on-top-Fe O_2 configuration, the two Fe−O distances and the O−O bond length are 1.84, 1.87, and 1.39 Å, respectively. A comparison of the calculated O−O bond length for the adsorbed O_2 with that of the gas phase O_2 (1.24 Å) suggests softening of the adsorbed O−O bonds and this is confirmed by our calculated lower O−O stretching vibrational frequency of the adsorbed O_2 (**Table 2**) compared to the gas phase molecule. The O−O stretching vibrational frequencies for O_2 adsorbed end-on at bridge-Fe and top-Fe sites, and side-on at top-Fe-site are assigned to 1087.5, 1069.4, and 984.9 cm^{-1}, respectively. Based on the calculated stretching frequencies and the O−O bond lengths of the adsorbed O_2 (1.30−1.39 Å) which is similar to that of the O_2^- ion (1.33 Å),[47, 85] we would suggest that the adsorbed molecular oxygen species on the FeS{011} surface are superoxo (O_2^-) species.

In order to ascertain the extent of oxidation of the interacting surface Fe ions on the FeS{011} surface upon oxygen adsorption, we have determined their ionic charges and compared them to those on the clean surface. We find that the Fe atoms to which both atomic and molecular oxygen are bound become more positive (1.13−1.20 e^-) compared to the clean surface Fe charge of +0.87 e^-, which from the qFe^{2+}/qFe^{3+} ratio is enough to suggest that they have been oxidized from Fe^{2+} to Fe^{3+}. This is consistent with the significant charge drawn from these surface Fe sites by the adsorbed atomic and molecular oxygen. The charge gained by the O_2 molecule upon adsorption end-on at bridge-Fe, top-Fe; and side-on at top-Fe sites is calculated to be 0.48 e^-, 0.57 e^- and 0.76 e^-, respectively, and the charge gained by the atomic O adsorbed at the top- and bridge-Fe sites is calculated to be 0.67 e^- and 0.63 e^-, respectively. The significant charge gained by the O_2 molecule upon adsorption, which

characterizes it as a superoxide (O_2^-), is responsible for the elongation of the O−O bond lengths (1.30−1.39 Å) reported. A number arlier ab-initio calculations,[31, 47, 68] have also identified the formation of a superoxide *via* electron transfer from pyrite surface Fe species.

We have investigated the nature of interaction of the identified superoxide form of O_2 on the FeS(011) surface by analysing the partial density of states (pDOS) projected on the interacting surface Fe *d*-states and O *p*-state as shown in the **Figure 6**. We observe strong hybridization between the interacting Fe *d*-states and O *p*-states, which is characterised by charge transfer from the interacting Fe ions into the adsorbed oxygen π_g orbital as revealed by the isosurface plot of the differential charge density (inserts in **Figure 6**). The structural changes in the adsorbed O_2 suggest that these molecular states are likely precursors for O_2 dissociation. The O−O bond of the energetically most favourable side-on O_2 adsorption configuration is found to readily break into atomic O adsorbed at two adjacent Fe sites (see **Figure 5D1**). Relative to the molecular adsorption state, the dissociation process is found to be highly exothermic with a calculated reaction energy of E_r = −1.96 eV, with an activation energy barrier of only E_a = 0.37 eV, suggesting that O_2 will readily dissociate at the FeS{011} surface even at low temperatures.

3.5 Water adsorption and dissociation on clean and O-covered FeS{001}

The most stable adsorption configuration of water on the clean FeS{001} is shown in **Figure 7a**, whereas the adsorption energies, equilibrium interatomic distances, and O–H stretching vibrational modes are listed in **Table 3**. It is found that the water molecule interacts weakly with the {001} surface, with the hydrogen atoms pointing toward surface sulfur atoms, releasing an adsorption energy of 0.17 eV. The shortest interatomic distance between the interacting S and H atoms (S−H) is calculated at 2.679 Å. Consistent with the weak

interaction, we observe no significant changes in the geometrical parameters of the adsorbed molecule compared to the gas phase paramters, and no charge transfer is observed.

Dissociative adsorption of H_2O on the clean FeS{001} surface is found to be highly endothermic (2.14 eV), and an energy barrier of 1.73 eV has to overcome to produce the dissociation products (OH + H pair adsorbed at top-S site). The preference for molecular to dissociative adsorption of water can be attributed to the fact that breaking a very strong O–H bond requires much more energy than the energy released in the formation of the weaker S–H and S–OH bonds on the {001} surface. By contrast, on several oxide surfaces the dissociative state of H_2O is thermodynamically stable than the molecularly adsorbed state, e.g., on Al_2O_3, TiO_2, etc., because the breaking of an O–H bond is effectively balanced by the formation of a metal–O and another O–H bond with a surface oxygen.[84] The schematic representations of the initial, transition, and final states of the dissociaition of water on the clean FeS{001} surface are shown in **Figure 8a**.This result indicates that without the presence of promoters, e.g., OH and O species on the surface, water on the clean FeS{001} surface will remain molecularly adsorbed. We have therefore investigated the adsorption and dissociation characteristics of water on pre-adsorbed O−FeS{001} surface. Two co-adsorption structures between H_2O and an O atom pre-adsorbed at top-S (**Figure 7b**) and 4-fold-bridge-Fe (**Figure 7c**) sites have been investigated. The co-adsorption energies between the H_2O and O on the FeS surface is calculated as follows:

$$E_{co-ads} = E_{(H_2O+O)/FeS(slab)} - (E_{FeS(slab)} + E_{H_2O} + \frac{1}{2}E_{O_2}) \quad (2)$$

where E_{H_2O}, E_{O_2}, $E_{FeS(slab)}$, and $E_{(H_2O+O)/FeS(slab)}$ are the total energy for the free molecule of water, molecular oxygen, the clean FeS slab, and the co-adsorbed (H_2O+O)/FeS slab systems, respectively. The most favorable co-adsorbed configuration of the (H_2O+O)/FeS system is found to be the structure with one of the hydrogen atoms pointing toward the pre-adsorbed O

atom on top-S site (**Figure 7b**). The co-adsorption energies calculated for H_2O and O pre-adsorbed at top-S and 4-fold-bridge-Fe sites are −1.23 eV and −0.29 eV, respectively, comparable to the sum of the separate adsorption energies of −1.19 eV an −0.28 eV. The co-adsorption energies are slightly more negative than the sum of the separate adsorption energies, which indicates an attractive interaction between the two species on the FeS{001} surface. In contrast to the highly endothermic dissociative adsorption process obtained for water on the clean FeS{001}, the dissociative adsorption of water on the oxygen covered FeS{001} surface is found to be slightly exothermic (−0.05 eV) and the energy barrier for dissociating the O−H bond in H_2O is greatly reduced by 0.54 eV in the presence of an O atom, suggesting that the pre-adsorbed oxygen atom could facilitate the dissociation of H_2O on FeS{001} surface into two zero-valent sulfur-hydroxyl, S^0−OH^-. The optimized structures for the initial, transition, and final states of the dissociation of H_2O in the presence of pre-adsorbed O on FeS{001} surface are shown in **Figure 8b**.

3.6 Water adsorption and dissociation on clean and O-covered FeS{011}

The most stable adsorption structure of water on the clean FeS{011} is shown in **Figure 9a**, wherein the water molecule adsorbs at an Fe site *via* the oxygen atom, releasing an adsorption energy of −0.68 eV. Similar adsorption characteristics were reported for molecularly adsorbed water on the pyrite {100} surface; Stirling *et al.*[46] and Sit *et al.*[47] reported adsorption energies of −0.56 eV and −0.68 eV respectively, for water on pyrite {100} surface from their DFT calculations. The adsorbed H_2O molecule is best characterized as physisorbed on the {011} surface since the sum of the charge gained by the H_2O molecule is 0.03 e^-, indicating negligible charge transfer. In agreement with the relatively small charge transfer, the charge of the surface Fe ion bound to water becomes only slightly more positive (+0.93 e^-) compared to the clean surface charge of +0.87 e^-, but not enough to suggest that its

formal oxidation state should be considered Fe^{3+}. The oxygen to surface Fe distance (Fe−O) is calculated at 2.185 Å, with the O−H bond length slightly elongated (0.972→0.981 Å) and the α(H-O-H) bond angle increased from 104.7° to 105.3°, indicating that the O−H bond is somewhat activated. The stretched O−H bonds are further confirmed via vibrational frequency calculations, where the asymmetric (υ_{as}) and symmetric (υ_{s}) stretching vibrational modes are calculated at 3653.2 and 3554.5 cm^{-1}, respectively. When compared with the calculated (3713 and 3623 cm^{-1}) and experimental[81] values (3742 and 3650cm^{-1}) of the gas phase H_2O molecule, this represents a reduction, confirming softening of the O−H bonds.

The stretched O−H bond suggests that it might break to produce surface proton and hydroxyl fragments. We have investigated this scenario but found that the dissociative adsorption of water on the clean FeS{011} surface is slightly endothermic by 0.18 eV relative to the associative molecular adsorption. The activation energy required for water dissociation on the clean FeS{011} surface is calculated at 0.83 eV, which is higher than the absolute value of the water adsorption energy (0.68 eV). Water dissociation is therefore not expected on the clean FeS{011} surface without the presence of promoters, e.g., OH and O species, on the surface, similar to the results obtained on pyrite the {100} surface.[46] The representations of the initial (IS), transition (TS), and final (TS) states for the most favorable reaction paths are shown in **Figure 10a**.

Next, we have investigated the adsorption and dissociation of water on the FeS{011} surface with pre-adsorbed atomic oxygen. Two co-adsorption systems have been explored with the H_2O and O co-adsorbed at (1) neighbouring surface Fe sites (distance between H and pre-adsorbed O atom is 2.675 Å), and (2) more remote surface Fe sites (distance between H and pre-adsorbed O atom is 6.058 Å). The optimized adsorption geometries of water co-adsorbed with O at neighbouring and remote surface Fe sites are shown in **Figure 9 (b & c)**, respectively, whereas the co-adsorption energies and the relevant optimized geometric

parameters are summarized in **Table 3**. When water is co-adsorbed with O at remote Fe sites, the co-adsorption energy is calculated at −2.53 eV, which is very close to the sum of the separate adsorption energies (−2.57 eV), suggesting minimal interaction between the two adsorbates. However, when water is co-adsorbed with O at neighbouring Fe sites, the co-adsorption energy is calculated to be −3.31 eV, which is significantly more negative than the sum of the separate adsorption energies (−2.43 eV), suggesting strong interaction between the two adsorbates, which gave rise to spontaneous proton transfer from the water to the O atom, resulting in the formation of ferric hydroxyl species (**Figure 9b**). In contrast to the water dissociation on the clean FeS{011} surface, the spontaneous proton transfer reaction on the pre-covered O-FeS{011} surface is exothermic by 0.88 eV, relative to the sum of the separate adsorption energies of water and atomic O, and needs to overcome only a very small barrier of 0.14 eV, which is 0.74 eV lower than that of 0.83 eV on the clean FeS{011} surface. This obvious lowering of the energy barrier suggests that the pre-adsorbed oxygen atom contributes prominently to the dissociation of H_2O on the FeS{011} surface. The structures of the transition and final states for the dissociation process are shown in **Figure 10b**. Similar results have been observed on the Au(111)[82] and Pd(100)[83] surfaces, where the surfaces were shown to readily promote the dehydrogenation of water when pre-covered with oxygen, which did not occur on the clean surfaces.

Regarding the extent of oxidation of the interacting surface Fe ions, when H_2O and O are co-adsorbed at remote Fe sites, we find that the charge of the Fe atoms bound to water (1.00 e^-) and dioxygen (1.20 e^-) suggests that the atomic oxygen oxidizes the interacting Fe ion more than water. The proton transfer from the H_2O to the pre-adsorbed O thereby producing two OH^- species, when co-adsorbed at neighbouring Fe sites, results in the charge of the Fe atoms bound to the OH^- species to become more positive (+1.18 e^-), compared to the clean surface Fe charge of 0.87 e^-. From the qFe^{2+}/qFe^{3+} ratio is enough to suggest a

formal Fe^{3+}oxidation states. Consistently, the spin density isosurface plot (**Figure 11**) also show larger spin density localization at the interacting Fe sites which are oxidised to Fe^{3+} compared to the non-interacting Fe sites which remain at Fe^{2+} states.

IV. SUMMARY AND CONCLUSIONS

We have investigated the adsorption and dissociation reactions of oxygen and water on the {001} and {011} surfaces of mackinawite, using the dispersion corrected DFT-D2 aproach. Our results show that, while water interacts only weakly with both FeS surfaces, the atomic and molecular oxygen interacts strongly with the surface cations on the {011} surface by drawing significant charge from them, causing them to be oxidized from Fe^{2+} to Fe^{3+}. The adsorption of atomic O at S sites on the {001} surface is also characterized by significant charge transfer to adsorbed O, resulting in significant oxidation of the intearacting S ion which becomes positively charged (+0.95 e^-) compared to its negative charge of −0.81 e^- in the clean surface. The adsorbed O_2 molecule exhibits characteristics of a superoxide (O_2^-) with elongated O–O bond distance, confirmed by our calculated O–O stretching vibrational frequency. When we compare the adsorption and dissociation of H_2O on the clean and on oxygen-covered FeS surfaces, we find that the O–H bond could be activated by O_{ads}, which plays a key role in the dissociation reaction of water. Our results provide fundamental and general insight into the adsorption processes and mechanisms of the early oxidation of mackinawite in the presence of oxygen and water, which may stimulate further experimental research.

ACKNOWLEDGMENTS

We acknowledge the Netherlands Foundation for Fundamental Research on Matter (FOM) for funding (Grant No. 13CO26-2). This work made use of the facilities of ARCHER (http://www.archer.ac.uk), the UK's national supercomputing service *via* our membership of the UK's HEC Materials Chemistry Consortium, which is funded by EPSRC (EP/L000202).

REFERENCES

1. Ennaoui, A.; Fiechter, S.; Jaegermann, W.; Tributsch, H. Photoelectrochemistry of Highly Quantum Efficient Single-Crystalline n - FeS2 (Pyrite). *J. Electrochem. Soc*. **1986**, 133, 97−106.
2. Macpherson, H.A.; Stoldt, C.R. Iron Pyrite Nanocubes: Size and Shape Considerations for Photovoltaic Application. *ACS Nano,* **2012**, 6, 8940–8949.
3. Ennaoui, A.; Fiechter, S.; Pettenkofer, Ch.; Alonso-Vante, N.; Bülker, K.; Bronold, M.; Höpfner, Ch.; Tributsch, H. Iron disulfide for solar energy conversion. *Solar Energy Materials and Solar Cells* **1993**, 29, 289−370.
4. Puthussery, J.; Seefeld, S.; Berry, N.; Gibbs, M.; Law, M. Colloidal Iron Pyrite (FeS_2) Nanocrystal Inks for Thin-Film Photovoltaics. *J. Am. Chem. Soc.*, **2011**, 133, 716–719.
5. Ennaoui, A.; Tributsch, H. Energetic characterization of the photoactive FeS_2 (pyrite) interface. *Solar Energy Materials* **1986**, 14, 461−474.
6. Namanu, P.; Jayalakshmi, M.; Bhat, K.U. Low temperature synthesis of iron pyrite nanorods for photovoltaic applications. *J. Mater. Sci.: Mater. Electron.* **2015**, 26, 8534–8539.
7. Bi, Y.; Yuan, Y.; Exstrom, C.L.; Darveau, S. A.; Huang, J. Air Stable, Photosensitive, Phase Pure Iron Pyrite Nanocrystal Thin Films for Photovoltaic Application. *Nano Lett.*, **2011**, 11, 4953–4957.
8. Xia, J.; Jiao, J.; Dai, B.; Qiu, W.; He, S.; Qiu, W.; Shen, P.; Chen, L. Facile synthesis of FeS_2 nanocrystals and their magnetic and electrochemical properties. *RSC Adv.*, **2013**, 3, 6132–6140.
9. Kim, B-C.; Takada, K.; Ohta, N.; Seino, Y.; Zhang, L.; Wada, H.; Sasaki, T. All solid state Li-ion secondary battery with FeS anode. *Solid State Ionics* **2005**, 176, 2383−2387.

10. Kendrick, E.; Barker, J.; Bao, J.; Świątek, A. The rate characteristics of lithium iron sulfide. *Journal of Power Sources* **2011**, 196, 6929–6933.
11. Roldan, A.; Hollingsworth, N.; Roffey, A.; Islam, H.-U.; Goodall, J. B. M.; Catlow, C. R. A.; Darr, J. A.; Bras, W.; Sankar, G.; Holt, K. B.; Hogarth, G.; de Leeuw, N. H. Bio-Inspired CO_2 Conversion by Iron Sulfide Catalysts under Sustainable Conditions. Chem. Commun. **51**, 7501−7504 (2015).
12. Dzade, N.Y.; Roldan, A.; de Leeuw, N.H. The surface chemistry of NOx on mackinawite (FeS) surfaces: A DFT-D2 study. *Phys. Chem. Chem. Phys*. **2014**, 16, 15444−15456.
13. Varley, J.B.; Hansen, H.A.; Ammitzbøll, N.L.; Grabow, L.C.; Peterson, A.A.; Rossmeisl, J.; Nørskov, J. K. Ni-Fe-S Cubanesin CO_2 Reduction Electrocatalysis: A DFT Study. *ACS Catal.* **2013**, 3, 2640−2643
14. Dzade, N.Y.; Roldan, A.; de Leeuw, N.H. Activation and dissociation of CO_2 on the (001), (011), and (111) surfaces ofmackinawite (FeS): A dispersion-corrected DFT studyN.H. J. Chem. Phys. **2015**, 143, 094703.
15. Dzade, N.Y.; Roldan, A.; de Leeuw, N.H. DFT-D2 simulations of water adsorption and dissociation on the low-index surfacesof mackinawite (FeS). *J. Chem. Phys*. **2016**, 144, 174704
16. Haider, S.; Roldan, A.; de Leeuw, N. H. Catalytic Dissociation of Water on the (001), (011), and (111) Surfaces of Violarite, $FeNi_2S_4$: A DFT-D2 Study. *J. Phys. Chem. C*, **2014**, 118, 1958−1967.
17. Huber, C.; Wächtershäuser, G. Activated acetic acid by carbon fixation on (Fe,Ni)S under primordial conditions. *Science*, **1997**, 276, 245−247.
18. Huber, C.; Wächtershäuser, G. Peptides by activation of amino acids with CO on (Ni,Fe)S surfaces: Implications for the origin of life. *Science* **1998**, 281, 670−672.
19. Wächtershäuser, G. Groundworks for an evolutionary biochemistry: the iron-sulphur world. Biophys. *Molec. Biol*., **1992**, 58, 85−201.
20. Wächtershäuser, G. Before enzymes and templates: theory of surface metabolism. *Microbiological Reviews*, **1988**, 52, 452−484.
21. Russell, M.J.; Hall, A. J. The emergence of life from iron monosulphide bubbles at a submarine hydrothermal redox and pH front. *J Geol Soc London*. **1997**, 154, 377−402.

22. Blöchl, E.; Keller, M.; Wächtershäuser, G.; Stetter, K.O. Reactions depending on iron sulfide and linking geochemistry with biochemistry. *Proc. Natl. Acad. Sci. USA* **1992**, 89, 8117−8120.
23. Watson, J.H.P.; Cressey, B.A.; Roberts, A.P.; Ellwood, D.C.; Charnock, J.M.; Soper, A.K. Structural and magnetic studies on heavy-metal-adsorbing iron sulphide nanoparticles produced by sulphate-reducing bacteria. *J. Magn. Magn. Mater*. **2000**, 214, 13−30.
24. Wolthers, M.; Charlet, L.; van Der Weijden, C.H.; van der Linde, P.R.; Rickard, D. Arsenic mobility in the ambient sulfidic environment: Sorption of arsenic(V) and arsenic(III) onto disordered mackinawite. *Geochim. Cosmochim. Acta*. **2005**, 69, 3483–3492.
25. Scheinost, A.C.; Charlet, L. Selenite reduction by mackinawite, magnetite and siderite: XAS characterization of nanosized redox products. *Environ. Sci. Technol.* **2008**, 42, 1984−1989.
26. Livens, F.R.; Jones, M.J.; Hynes, A.J.; Charnock, J.M.; Mosselmans, J.F.; Hennig, C.; Steele, H.; Collison, D.; Vaughan, D.J.; Pattrick, R.A.; Reed, W.A.; Moyes, L.N. X-ray absorption spectroscopy studies of reactions of technetium, uranium and neptunium with mackinawite. *J. Environ. Radioact*. **2004**, 74, 211−219.
27. Mullet, M.; Boursiquot, S.; Ehrhardt, J.J. Removal of hexavalent chromium from solutions by mackinawite, tetragonal FeS. *Colloid Surface A*, **2004**, 244, 77−85.
28. Rickard, D.; Luther, G.W. Chemistry of Iron Sulfides. *Chemical Reviews*, **2007**, 107, 514–562.
29. Benning, L.G.; Wilkin, R.T.; Barnes, H.L. Reaction pathways in the Fe–S system below 100°C. *Chemical Geology* **2000**, 167, 25–51.
30. Berner, R.A. Iron Sulfides Formed from Aqueous Solution at Low Temperatures and Atmospheric Pressure J. Geol. **1964**, 72, 293–306.
31. Lennie, A.R.; Redfern, S.A.T.; Champness, P.E.; Stoddart, C.P.; Schofield, P.F.; Vaughan, D.J. Transformation of mackinawite to greigite: An in situ X-ray powder diffraction and transmission electron microscope study. *Am. Mineral*. **1997**, 82, 302–309.
32. Rosso, K.M.; Becker, U.; Hochella, M.F. Atomically resolved electronic structure of pyrite {100} surfaces: An experimental and theoretical investigation with implications for reactivity. *Amer. Miner*. **1999**, 84, 1535–1548.

33. Buckley, A.N.; Woods, R. The surface oxidation of pyrite. *Appl. Surf. Sci.* **1987**, 27, 437–452.
34. Raikar, G.N.; Thurgate, S.M.; An Auger and EELS study of oxygen adsorption on FeS_2. *J. Phys.- Condens. Matter*, **1991**, 3, 1931–1939.
35. Bourdoiseau, J.-A.; Jeannin, M.; Sabot, R.; Rémazeilles, C.; Refait, P. Characterisation of mackinawite by Raman spectroscopy: effects of crystallisation, drying and oxidation. *Corrosion Science*, **2008**, 50, 3247–3255.
36. Nesbitt, H.W.; Muir, I.J.; X-ray photoelectron spectroscopic studies of a pristine pyrite surface reacted with water vapour and air. *Geochim. Cosmochim. Acta*, **1994**, 58, 4667–4679.
37. Guevremont, J.M.; Strongin, D.R.; Schoonen, M.A.A. Effects of surface imperfections on the binding of CH_3OH and H_2O on FeS_2 (100): Using adsorbed Xe as a probe of mineral surface structure. Surf. Sci. **391**, 109–124 (1997).
38. Guevremont, J.M.; Strongin, D.R.; Schoonen, M.A.A. Photoemission of adsorbed Xenon, X-ray photoelectron spectroscopy, and temperature-programmed desorption studies of H_2O on FeS_2 (100). *Langmuir* **1998**, 14, 1361–1366.
39. Schoonen, M.; Elsetinow, A.; Borda, M.; Strongin, D. Effect of temperature and illumination on pyrite oxidation between pH 2 and 6. Geochem. Trans., **2000**, 1, 23−33
40. Andersson, K.; Nyberg, M.; Ogasawara, H.; Nordlund, D.; Kendelewicz, T.; Doyle, C.S.; Brown Jr., G.E.; Pettersson, L.G.M.; Nilsson, A. Experimental and theoretical characterization of the structure of defects at the pyrite FeS_2(100) surface. *Phys. Rev. B*, **2004**, 70, 195404.
41. Eggleston, C.M.; Ehrhardt, J.J.; Stumm. W. Surface structural controls on pyrite oxidation kinetics: An XPS-UPS, STM, and modeling study. *Am. Mineral*., **1996**, 81, 1036–1056.
42. Eggleston, C.M. Initial oxidation of sulfide sites on a galena surface: Experimental confirmation of an ab-initio calculation. *Geochim. Cosmochim. Acta*, **1997**, 61, 657–660.
43. Dos Santos, E.C.; de Mendonça Silva, J.C.; Duarte, H.A. Pyrite Oxidation Mechanism by Oxygen in Aqueous Medium. *J. Phys. Chem. C* **2016**, 120, 2760−2768
44. Zhang, Y.N.; Hu, J.; Law, M.; Wu, R.Q.; Effect of surface stoichiometry on the band gap of the pyrite FeS_2(100) surface. *Phys. Rev. B*, **2012**, 85, 085314.

45. Hu, J.; Zhang, Y.; Law, M.; Wu, R. First-principles studies of the electronic properties of native and substitutional anionicdefects in bulk iron pyrite. *Phys. Rev. B*, **2012**, 85, 085203.
46. Stirling, A.; Bernasconi, M.; Parrinello, M. Ab initio simulation of water interaction with the (100) surface of pyrite. *J. Chem. Phys.* **2003**, 118, 8917.
47. Sit, P.H.-L.; Cohen, M.H.; Selloni, A. Interaction of oxygen and water with the (100) surface of pyrite: mechanism of sulfur oxidation. *J. Phys. Chem. Lett*. **2012**, 3, 2409–2414.
48. Nguyen, H.T.; Nguyen, M.T. Effects of Sulfur-Deficient Defect and Water on Rearrangements of Formamide on Pyrite (100) Surface. *J. Phys. Chem. A* **2014**, 118, 4079−4086.
49. de Leeuw, N.H.; Parker, S. C.; Sithole, H. M.; Ngoepe, P. E. Modeling the surface structure and reactivity of pyrite: Introducing a potential model for FeS_2. *J. Phys. Chem. B*, **2000**, 104, 7969–7976.
50. D. Santos-Carballal, A. Roldan, and N. H. de Leeuw, Early Oxidation Processes on the Greigite Fe_3S_4 (001) Surface by Water: A Density Functional Theory Study. *J. Phys. Chem. C*, **2016**, 120 (16), 8616–8629
51. Roldan, A.; de Leeuw, N. H. Catalytic water dissociation by greigite Fe3S4 surfaces: density functional theory study. *Proc. R. Soc*. **2016**, A 472, 20160080
52. Boursiquot, S.; Mullet, M.; Abdelmoula, M.; Génin, J.-M.; Ehrhardt, J.-J. The dry oxidation of tetragonal FeS_{1-x} mackinawite. *Phys. Chem. Minerals*, **28**, 600–611 (2001).
53. Kresse, G.; Hafner, Ab initio molecular dynamics for liquid metals. *J. Phys Rev B*, **1993**, 47, 558.
54. Kresse G.; Hafner, J. Norm-conserving and ultrasoft pseudopotentials for first-row and transition elements. *J Phys: Condens Matter*, **1994**, 6, 8245.
55. Kresse, G.; Furthmüller, Efficient iterative schemes for ab initio total-energy calculations using a plane-wave basis set. *J. Phys Rev B*, **1996**, 54, 11169.
56. Grimme, S. Semiempirical GGA-type density functional constructed with a long-range dispersion correction. *J Comput Chem*, **2006**, 27, 1787–1799.
57. Perdew, J. P.; Chevary, J. A.; Vosko, S.H.; Jackson, K.A.; Pederson, M.R.; Singh, D.J.; Fiolhais, C. Atoms, molecules, solids, and surfaces: Applications of the generalized gradient approximation for exchange and correlation. *Phys Rev B*, **1992**, 46, 6671.

58. Devey, A. J.; Grau-Crespo, R.; de Leeuw, N. H. Combined Density Functional Theory and Interatomic Potential Study of the Bulk and Surface Structures and Properties of the Iron Sulfide Mackinawite (FeS*). J. Phys, Chem C*, **2008**, 112, 10960–10967.
59. Monkhorst, H.J.; Pack, J.D. Special points for Brillouin-zone integrations. *Phys Rev B*, **1976**, 13, 5188.
60. Watson, G.W.; Kelsey, E.T.; de Leeuw, N.H.; Harris, D.J.; Parker, S.C. Atomistic simulation of dislocations, surfaces and interfaces in MgO. *J. Chem. Soc., Faraday Trans.*, **1996**, 92, 433–438.
61. Tasker, P.W. The stability of ionic crystal surfaces. *J. Phys. C: Solid State Phys*., **1979**, 12, 4977–4987.
62. Henkelman, G.; Arnaldsson, A.; Jonsson, H. A fast and robust algorithm for Bader decomposition of charge density. *Comput. Mater. Sci*. **2006**, 36, 354–360
63. Mills, G.; Jónsson, H.; Schenter, G.K. Reversible work transition state theory: application to dissociative adsorption of hydrogen. Surf. Sci. **1995**, **324**, 305–337.
64. Ulitsky, A.; Elber, R. A new technique to calculate steepest descent paths in flexible polyatomic systems. *J. Chem. Phys*. **1990**, 92, 1510–1511.
65. Lennie, A.R.; Redfern, S.A.T.; Schofield, P.F.; Vaughan, D.J. Synthesis and Rietveld Crystal Structure Refinement of Mackinawite, Tetragonal FeS. *Mineral. Mag*. **1995**, 59, 677–683.
66. Berner, R.A. Tetragonal Iron Sulfide. *Science*, **1962**, 137, 669.
67. Vaughan, D.J.; Craig, J.R. In Mineral Chemistry of Metal Sulfides, Cambridge University Press, New York, **1978**.
68. Rozgonyi, T.; Stirling, A. DFT study of oxidation states on pyrite surface sites. *J. Phys. Chem. C* **2015**, 119, 7704−7710
69. Jeong, H.Y., Lee, J.H., Hayes, K.F., Characterization of synthetic nanocrystalline mackinawite: crystal structure, particle size, and specific surface. *Geochim Cosmochim Acta*, **2008**, 72, 493–505.
70. Wolthers, M., van der Gaast, S. J, Rickard, D., The structure of disordered mackinawite. *Am. Mineral*., **2003**, 88, 2007–2015.
71. Dzade, N.Y.; Roldan, A.; de Leeuw, N. H. Adsorption of methylamine on mackinawite (FeS) surfaces: a density functional theory study. *J. Chem. Phys*. **2013**, 139, 124708.
72. Vaughan, D.J.; Ridout, M. S. Mössbauer studies of some sulphide minerals. *J Inorg Nucl. Chem*, **1971**, 33, 741–746.

73. Subedi, A.; Zhang, L.J.; Singh, D.J.; Du, M. H. Density functional study of FeS, FeSe, and FeTe: Electronic structure, magnetism, phonons, and superconductivity. *Phys. Rev. B.* 2008, 78, 134514.

74. Wittekindt, C.; Marx, D. Water confined between sheets of mackinawite FeS minerals. *J. Chem. Phys.* **2012**, 137, 054710.

75. Ohfuji, H.; Rickard, D. High resolution transmission electron microscopic study of synthetic nanocrystalline mackinawite. *Earth Planet. Sci. Lett*., **2006**, 241, 227–233.

76. Lide, D.R. In Handbook of Chemistry and Physics, 82nd ed., CRC Press, Boca Raton, **2001**.

77. Herzberg, G. Molecular Spectra and Molecular Structure. II. Infrared and Raman Spectra of Polyatomic Molecules, Lancaster Press, New York, **1946**, p.365.

78. Yoon, B.; Häkkinen, H.; Landman, U. Interaction of O_2 with gold clusters: Molecular and dissociative adsorption. *J. Phys. Chem. A*, **2003**, 107, 4066–4971.

79. Mattioli, G.; Filippone, F.; Bonapasta, A. A. Reaction intermediates in the photoreduction of oxygen molecules at the (101) TiO2 (anatase) surface. *J. Am. Chem. Soc*. **2006**, 128, 13772−13780.

80. CRC Handbook of Chemistry and Physics, 83rd ed., edited by D. R. Lide (CRC, New York, **2002**).

81. Shimanouchi, T. Tables of Molecular Vibrational Frequencies, Consolidated Volume II, NSRDS NBS-39, J. Phys. Chern. **1977**, 6, p.365.

82. Liu, R. Adsorption and dissociation of H_2O on Au(111) surface: A DFT study. *Computational and Theoretical Chemistry* 2013, 1019, 141−145.

83. Jiang, Z.; Li, L.; Li, M.; Li, R.; Fang, T. Density functional theory study on the adsorption and decomposition of H_2O on clean and oxygen-modified Pd (1 0 0) surface. *Appl. Surf. Sci.* **2014**, 301, 468–474

84. Thiel, P. A.; Madey, T.E. The interaction of water with solid surfaces: Fundamental aspects. Surf. Sci. Rep. **1987**, 7, 211−385.

85. Aschauer, U.; Chen, J.; Selloni A. Peroxide and superoxide states of adsorbed O_2 on anatase TiO_2 (101) with subsurface defects. *Phys. Chem. Chem. Phys*., **2010**, 12, 12956–12960

LIST OF TABLES

Table 1: Optimized structural parameters of mackinawite (FeS). A range of experimental unit cell parameters $a = b$, c and the c/a ratio are also given for comparison.

Parameter	Experiment[31,65, 66, 69, 70]	This work
$a=b$ /Å	3.650–3.679	3.587
c /Å	4.997–5.480	4.908
c/a	1.363–1.501	1.368
d(Fe−S) /Å	2.240–2.256	2.262
d(Fe–Fe) /Å	2.598–2.630	2.536

Table 2: Calculated adsorption energy (E_{ads}), charge (q), relevant bond distances (d) of atomic (O) and molecular (O_2) oxygen the {001} and {011} surfaces of FeS. The O−O stretching vibrational frequency (υ) of the adsorbed O_2 is also reported. The calculated gas phase d(O−O) =1.24 Å, and the υ(O−O) = 1545 cm^{-1}.

Surface	Adsorbate	Config.	E_{ads} /eV	$\|q\|$ /e^-	d(O−Fe) /Å	d(O−S) /Å	d(O−O) /Å	υ(O−O) /cm^{-1}
{001}	O	A1	−0.11	0.92	2.055	2.682	⎯⎯	⎯⎯
		A2	−1.02	1.85	3.200	1.491	⎯⎯	⎯⎯
	O_2	M1	+1.04	0.71	1.991	2.455	1.367	1006.6
		M2	−0.12	0.02	3.783	3.434	1.239	1495.0
		M3	−0.13	0.03	3.768	3.157	1.241	1494.3
		M4	−0.16	0.05	3.698	3.125	1.243	1489.1
		D1	−1.88	3.67	3.209	1.484	3.612	---
{011}	O	A1	−1.73	0.63	1.839	2.055	⎯⎯	⎯⎯
		A2	−1.89	0.67	1.616	3.091	⎯⎯	⎯⎯
	O_2	M1	−0.98	0.48	2.031	2.656	1.301	1187.5
		M2	−1.56	0.57	1.722	3.169	1.343	1069.4
		M3	−1.75	0.76	1.860	3.073	1.392	984.9
		D1	−3.71	1.34	1.607	3.057	3.491	⎯⎯

Table 3: Calculated adsorption energy (E_{ads}) and relevant bond distances (d) for H_2O adsorbed in isolation and co-adsorbed with atomic oxygen on FeS{001} and FeS{011} surfaces.

Surface	Adsorbate	E_{ads} /eV	d(O−H) /Å	d(Fe−O_{wat}) /Å	d(Fe−O_{oxy}) /Å	d(S−O_{oxy}) /Å	d(O_{oxy}−H) /Å
{001}	H_2O	−0.17	0.974	4.158	—	—	—
	H_2O + O on top-S	−1.23	0.984	3.804	3.194	1.503	1.941
	H_2O + O on bridge-Fe	−0.29	0.974	3.842	2.069	2.666	2.756
{011}	H_2O	−0.68	0.981	2.185	—	—	—
	H_2O + O: near	−3.31	1.817	1.848	1.776	—	1.002
	H_2O + O: remote	−2.49	0.980	2.180	1.618	3.107	6.246

LIST OF FIGURES

Figure 1: The layered structure of bulk FeS (a), with the tetragonal unit cell highlighted by dashed lines. The electronic density of state showing the total and projection on the Fe *d*-states and S *p*-states are shown in (b). (Colour scheme: Fe = grey, and S = yellow).

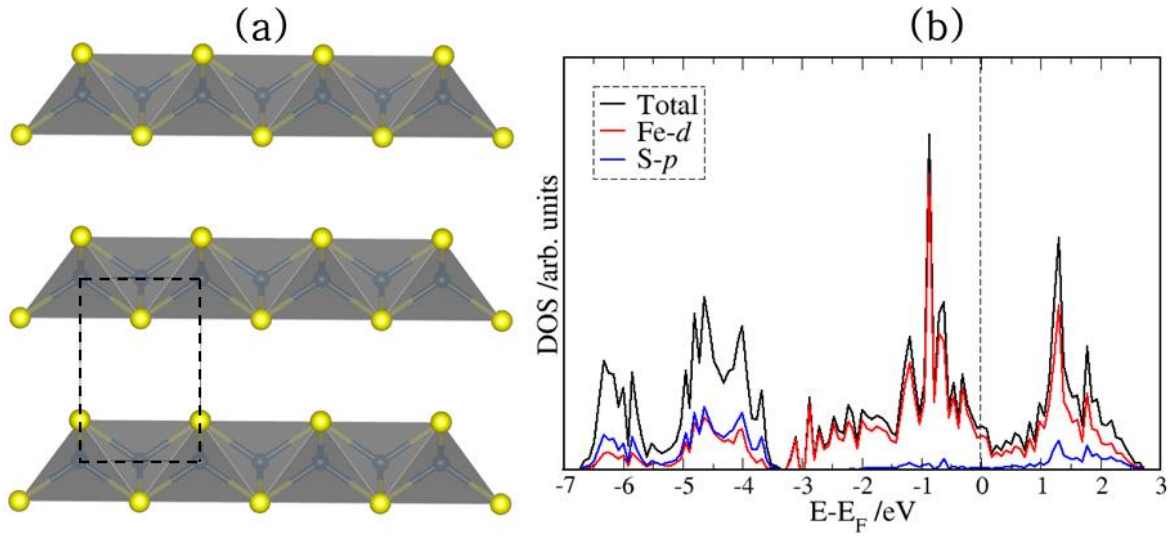

Figure 2: Schematic representation of the top and side views of the slab model of (a & b) FeS{001}−(2x2) and (c & d) FeS{011}−(3x1) supercells showing the corresponding different adsorption sites explored. (Colour scheme: Fe = grey, and S = yellow).

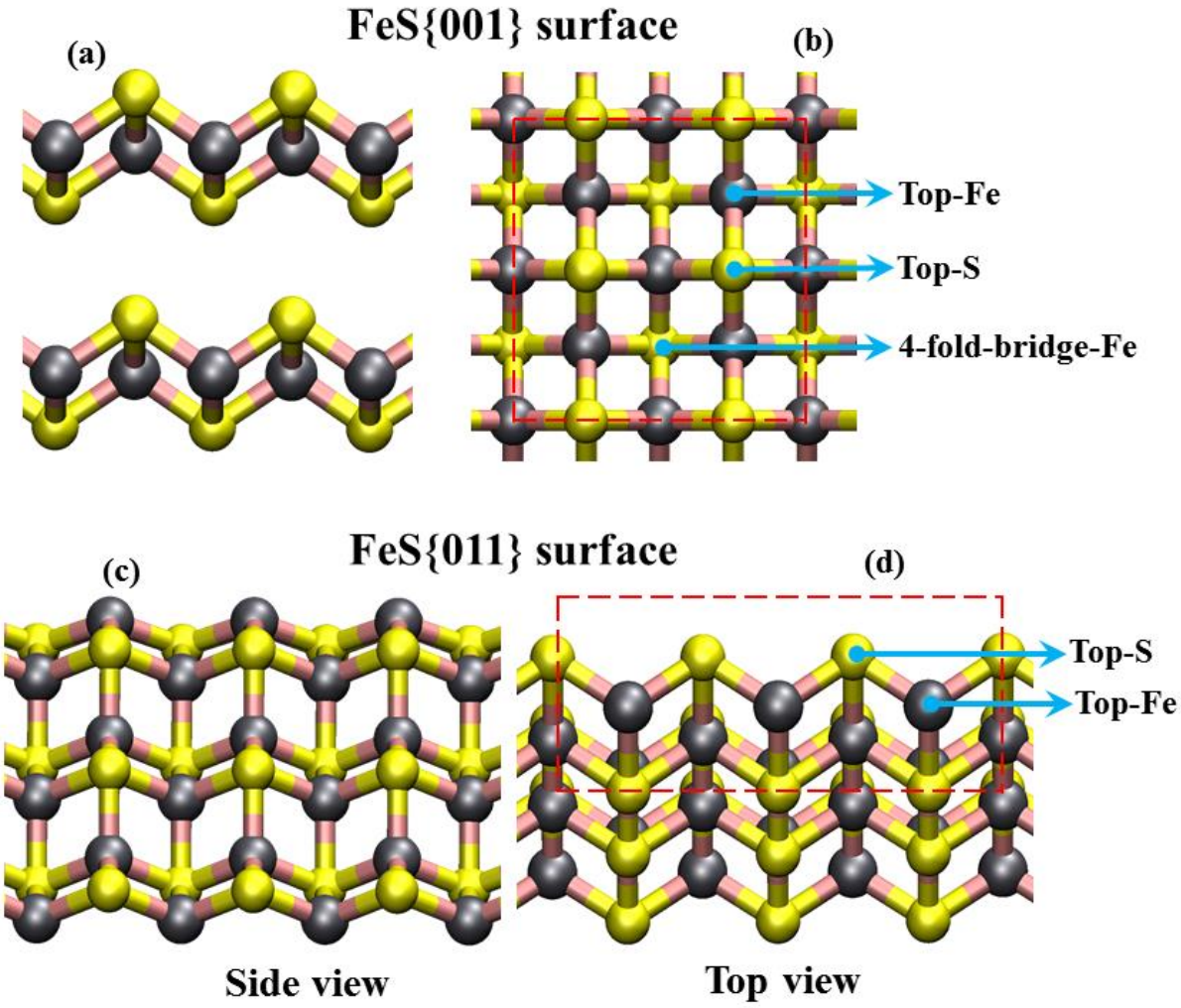

Figure 3: Side (top) and top (bottom) views of the relaxed adsorption structures of atomic oxygen adsorbed at 4-fold-bridge-Fe site (A1), top-S site (A2); molecular oxygen adsorbed side-on at top-Fe site (M1), head-on at top-S site (M2), head-on at 4-fold-bridge-Fe site (M3), side-on at 4-fold-bridge-Fe site (M4), and dissociated at adjacent top-S sites (D1), on the FeS{001} surface. (Colour scheme: Fe = grey, S = yellow, and O = red).

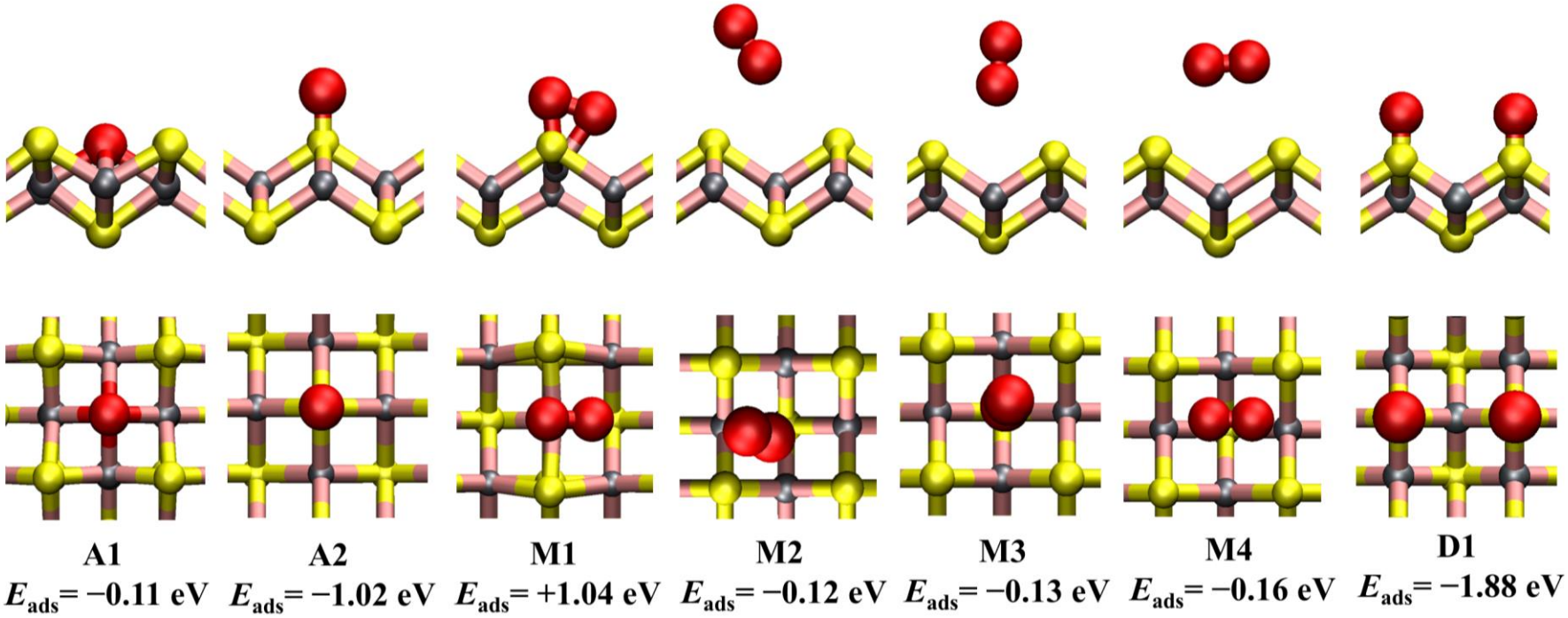

Figure 4: Partial DOS projected on the interacting surface S *p*-states and O *p*-states for adsorbed (a) atomic and (c) molecular oxygen. Shown in (b) and (d) are the corresponding isosurfaces of the differential charge density, where the green and red contours indicate electron density increase and decrease by 0.02 e/Å^3, respectively.

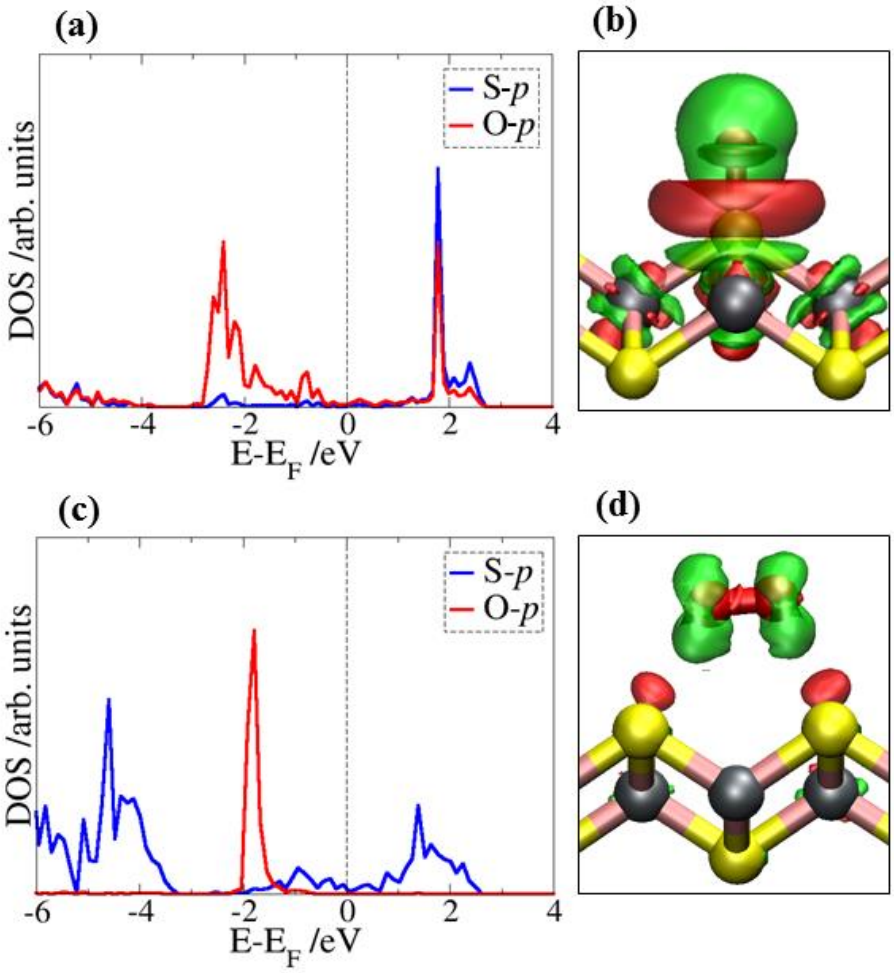

Figure 5: Top views of the relaxed adsorption structures of atomic oxygen adsorbed at (a) Fe-top and (b) bridge-Fe sites; molecular oxygen adsorbed in end-on configuration at (c) bridge-Fe, (d) top-Fe; side-on configuration at (e) top-Fe sites, respectively, on FeS{011} surface. (Colour scheme: Fe = grey, S = yellow, and O = red).

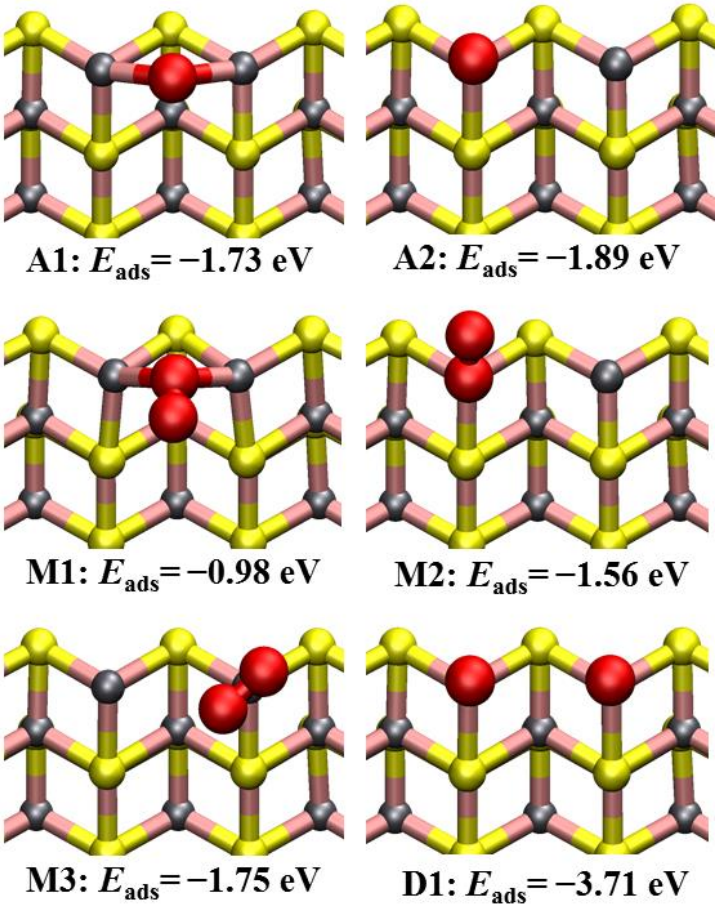

Figure 6: Partial DOS projected on the interacting surface Fe *d*-states and O *p*-states for adsorbed (a) atomic oxygen at top-Fe site; and molecular oxygen adsorbed in (b) end-on-bridge-Fe, (c) end-on-top-Fe, and (d) side-on-top-Fe configurations. The inserts show the corresponding isosurfaces of the differential charge density, where the green and red contours indicate electron density increase and decrease by 0.02 e/Å^3, respectively.

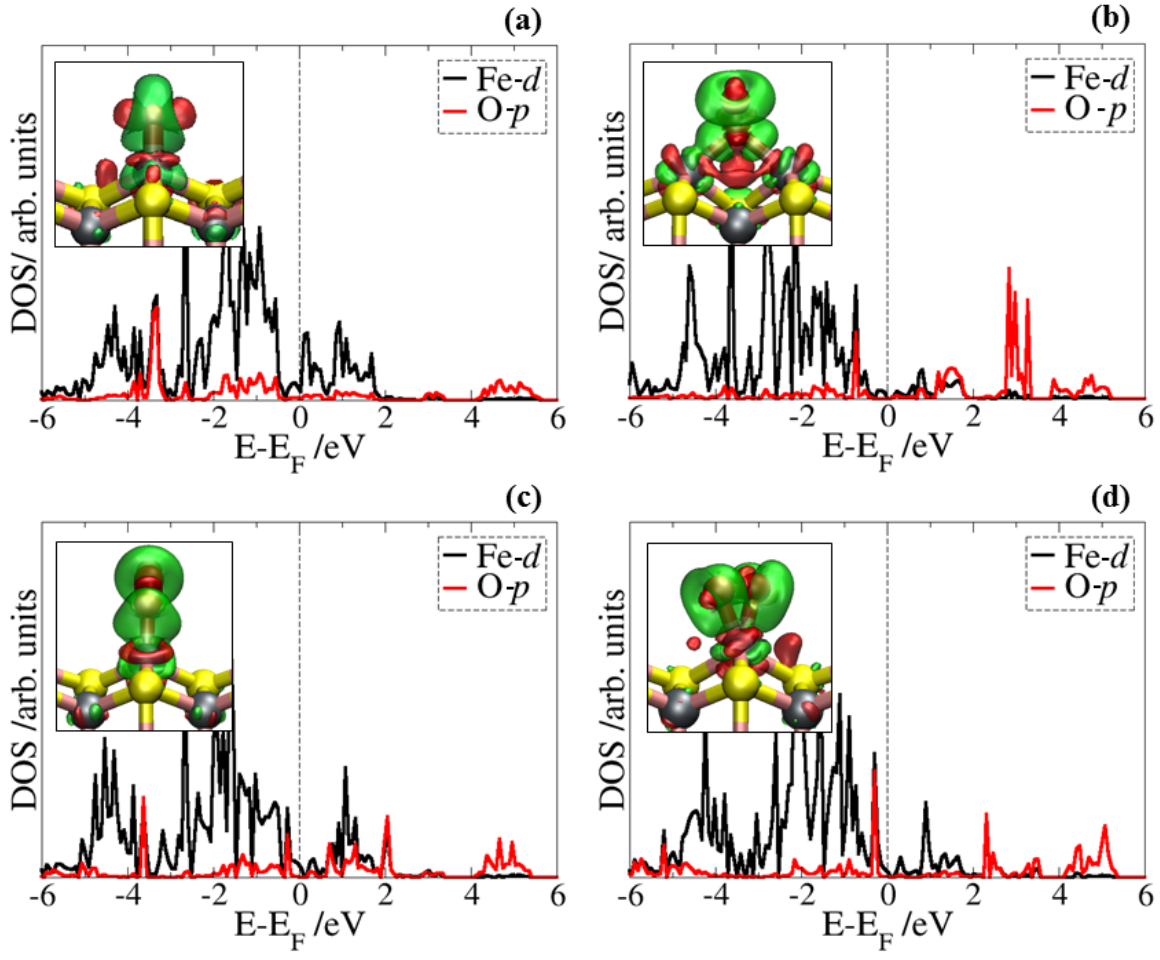

Figure 7: Side (top) and top (bottom) views of the relaxed adsorption structures of molecular H_2O (a); the co-adsorption structures of H_2O and pre-adsorbed O at (b) top S-site and (c) 4-fold Fe bridge-site on FeS{001} surface. (Colour scheme: Fe = grey, S = yellow, O = red, and H = white).

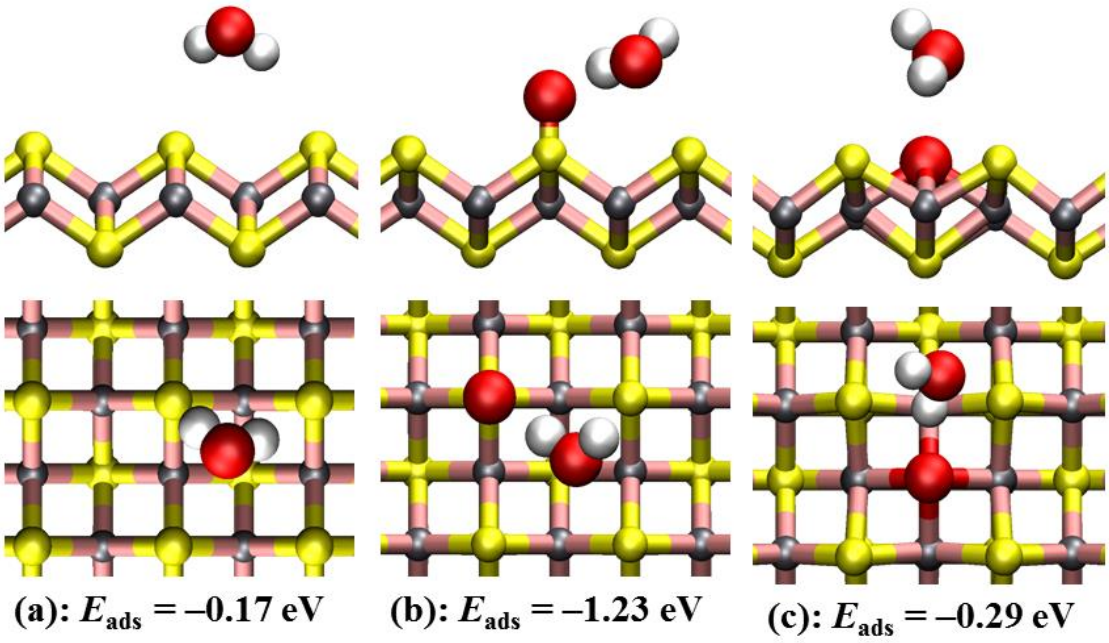

Figure 8: Optimized structures for the initial (IS, leftmost panels), transition (TS, central panels), and final (FS, rightmost panels) states of the most favorable path for the dissociation of: (a) H_2O, and (b) H_2O in the presence of pre-adsorbed O on FeS{001} surface. The length of the cleaved O−O and O−H bond is given in angstroms (Å). (Colour scheme: Fe = grey, S = yellow, O = red, and H = white).

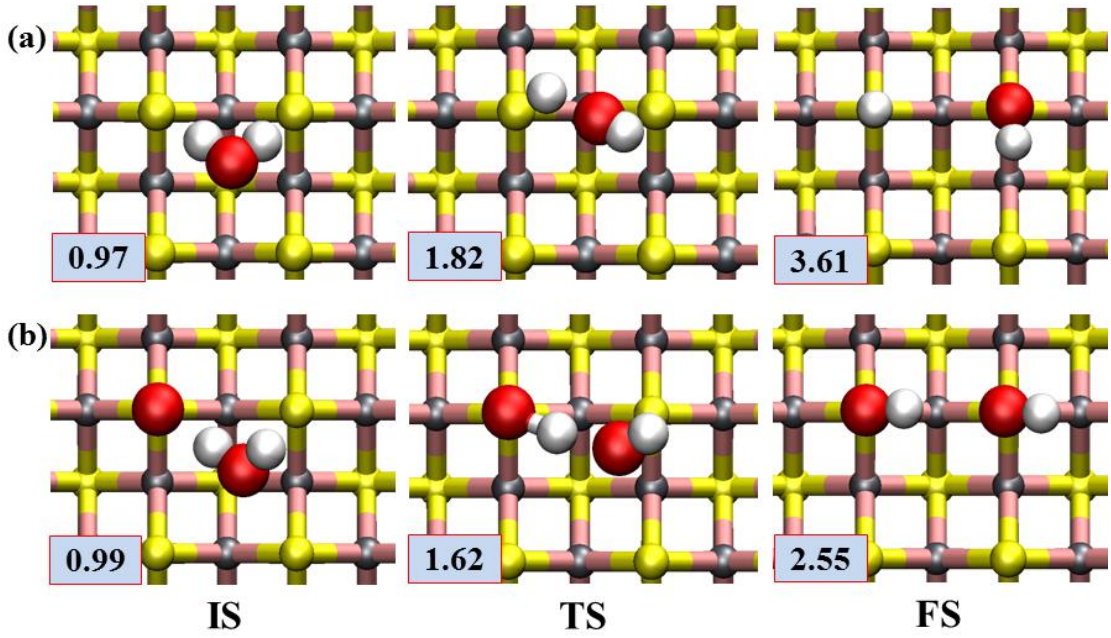

Figure 9: Side (top) and top (bottom) views of the relaxed adsorption structures of (a) molecular H_2O; the co-adsorption structures of H_2O and O at (b) neighbouring and (c) remote Fe sites on FeS{011} surface. (Colour scheme: Fe = grey, S = yellow, O = red, and H = white).

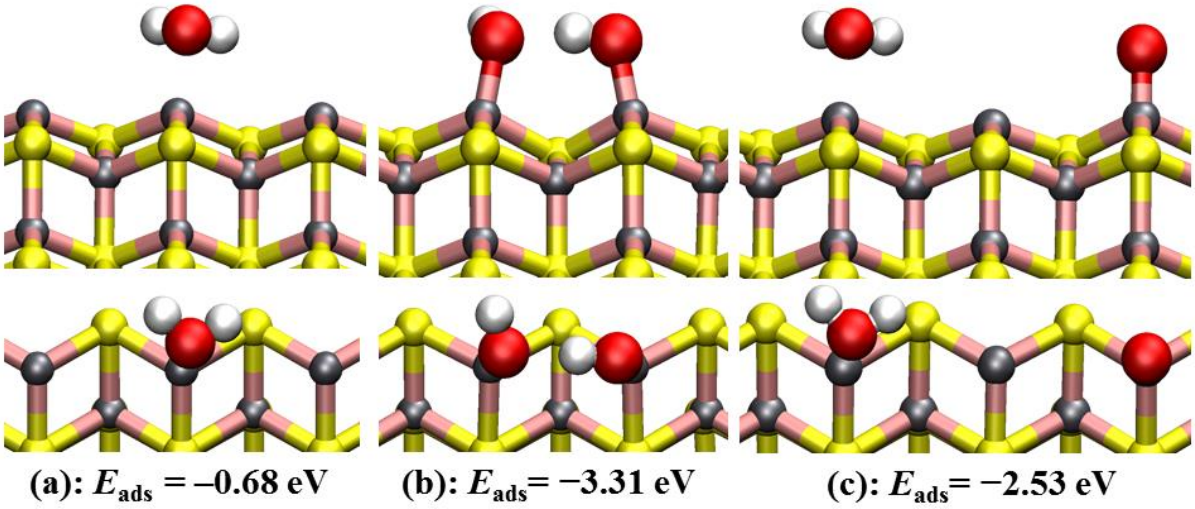

Figure 10: Optimized structures for the initial (IS, leftmost panels), transition (TS, central panels), and final (FS, rightmost panels) states of the most favorable path for the dissociation of: (a) H_2O, and (b) H_2O in the presence of pre-adsorbed O on FeS{011} surface. The length of the cleaved O−O and O−H bond is given in angstroms (Å). (Colour scheme: Fe = grey, S = yellow, O = red, and H = white).

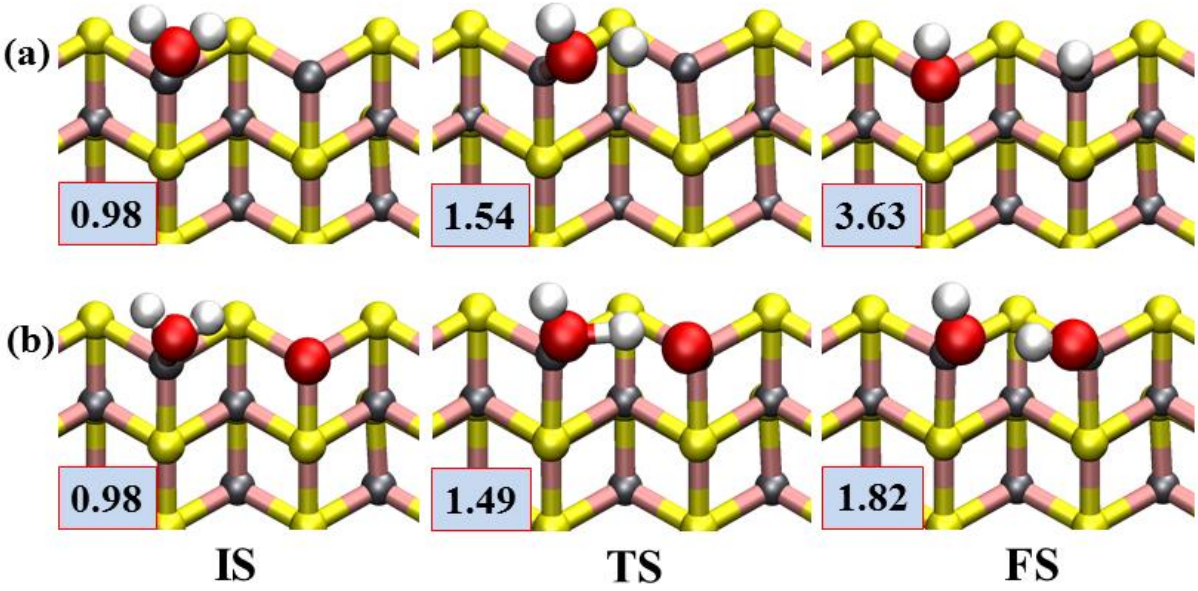

Figure 11: Spin density ($\rho = \rho\uparrow - \rho\downarrow$) isosurfaces of the co-adsorption structure of H_2O and O atom plotted at an iso-value of 0.02 e/Å^3.